

# Time-resolved smoothness of distributed brain activity tracks conscious states and unifies emergent neural phenomena

**Aditya Nanda**

Vanderbilt University

**Graham Johnson**

Vanderbilt University

**Yu Mu**

Chinese Academy of Science

**Misha Ahrens**

Janelia Research Campus, Howard Hughes Medical Institute <https://orcid.org/0000-0002-3457-4462>

**Catie Chang**

Vanderbilt University <https://orcid.org/0000-0003-1541-9579>

**Dario Englot**

Vanderbilt University Medical Center

**Michael Breakspear**

University of Newcastle, NSW <https://orcid.org/0000-0003-4943-3969>

**Mikhail Rubinov** (✉ [mika.rubinov@vanderbilt.edu](mailto:mika.rubinov@vanderbilt.edu))

Vanderbilt University

---

## Article

**Keywords:** brain-wide activity, electrocorticography, stereotactic EEG, calcium imaging, anesthesia, scale-free activity, critical dynamics, timeseries modeling

**Posted Date:** February 7th, 2022

**DOI:** <https://doi.org/10.21203/rs.3.rs-1195514/v2>

**License:** © ⓘ This work is licensed under a Creative Commons Attribution 4.0 International License.

[Read Full License](#)

---

# Time-resolved smoothness of distributed brain activity tracks conscious states and unifies emergent neural phenomena

Aditya Nanda<sup>1,\*</sup>,

Graham W Johnson<sup>1</sup>,

Yu Mu<sup>2</sup>,

Misha B Ahrens<sup>5</sup>,

Catie Chang<sup>1,3,4</sup>,

Dario J Englot<sup>1,6,7</sup>,

Michael Breakspear<sup>8,9</sup>,

Mikhail Rubinov<sup>1,4,3,\*</sup>

<sup>1</sup>Department of Biomedical Engineering, Vanderbilt University, USA

<sup>2</sup>Institute of Neuroscience, Center for Excellence in Brain Science and Intelligence Technology,  
Chinese Academy of Sciences, China

<sup>3</sup>Department of Electrical and Computer Engineering, Vanderbilt University, USA

<sup>4</sup>Department of Computer Science, Vanderbilt University, USA

<sup>5</sup>Janelia Research Campus, Howard Hughes Medical Institute, USA

<sup>6</sup>Department of Neurological Surgery, Vanderbilt University Medical Center, USA

<sup>7</sup>Department of Radiology and Radiological Sciences, Vanderbilt University Medical Center, USA

<sup>8</sup>School of Psychology, University of Newcastle, Australia

<sup>9</sup>School of Medicine and Public Health, University of Newcastle, Australia

\*Corresponding authors: [aditya.nanda@vanderbilt.edu](mailto:aditya.nanda@vanderbilt.edu), [mika.rubinov@vanderbilt.edu](mailto:mika.rubinov@vanderbilt.edu)

## Abstract

Much of systems neuroscience posits that emergent neural phenomena underpin important aspects of brain function. Studies in the field variously emphasize the importance of distinct emergent phenomena, including weakly stable dynamics, arrhythmic  $1/f$  activity, long-range temporal correlations, and scale-free avalanche statistics. Few studies, however, have sought to reconcile these often abstract phenomena with interpretable properties of neural activity. Here, we developed a method to efficiently and unbiasedly generate model data constrained by interpretable empirical features in long multiregional neurophysiological recordings. We used this method to ground several major emergent neural phenomena to time-resolved smoothness, the correlation of distributed brain activity between adjacent timepoints. We first found that in electrocorticography recordings, time-resolved smoothness closely tracked transitions between conscious and anesthetized states. We then showed that a minimal model constrained by time-resolved smoothness, variance, and mean, captured dynamical and statistical emergent neural phenomena across modalities and species. Our results thus decouple major emergent neural phenomena from network mechanisms of brain function, and instead couple these phenomena to spatially nonspecific, time-resolved changes of brain activity. These results anchor several theoretical frameworks to a single interpretable property of the neurophysiological signal and, in this way, ultimately help bridge abstract theories of brain function with observed properties of brain activity.

## 20 **Introduction**

Coordinated neuronal interactions give rise to intricate patterns of distributed brain activity. Much of systems neuroscience seeks to understand the spatiotemporal structure of these patterns. Studies often seek to explain this structure in terms of emergent neural phenomena, spatiotemporal patterns of brain activity that reflect complex interactions of individual neurons or brain regions. Many of these phenomena are situated within longstanding theoretical frameworks (Breakspear, 2017; Buzsáki, 2004; He, 2014; S. Palva & Palva, 2018). One such framework centers on the study of dynamical phenomena (Breakspear, 2017; Cunningham & Byron, 2014; Deco et al., 2011). Dynamical phenomena show up as trajectories in phase-space embeddings of neuronal (Churchland et al., 2012; Kato et al., 2015) or regional (Shine et al., 2019) recordings. These embeddings provide a convenient geometric representation of distributed brain activity (Saxena & Cunningham, 2019). Moreover, the smoothness of dynamical trajectories can endow dynamical activity with robustness to high-dimensional noise (Trautmann et al., 2019).

Another framework centers on the study of scale-free statistical phenomena. Scale-free phenomena lack typical sizes, durations, or frequencies (Buzsáki & Mizuseki, 2014; He, 2014; Roberts et al., 2015) and show up as heavy-tailed functions or distributions that resemble straight lines on log-log plots (Clauset et al., 2009). One example is the arrhythmic  $1/f$  activity of local field potentials (Donoghue et al., 2020; He et al., 2010). Another is the heavy-tailed distributions of sizes and durations of synchronous bursts or avalanches of neurons (Beggs & Plenz, 2003; Gireesh & Plenz, 2008; Hahn et al., 2010) and brain regions (Petermann et al., 2009; Shriki et al., 2013). Scale-free phenomena associate with long-range temporal correlations of neural activity (Linkenkaer-Hansen et al., 2001) and imply theoretically appealing function, including efficient representation of sensory input (Buzsáki & Mizuseki, 2014; Wohrer et al., 2013).

45 A third framework, the theory of neural criticality, lies at the intersection of the first two, and seeks to explain both dynamical and statistical emergent phenomena. This framework proposes that neural dynamics critically balance on the border of stable and unstable states (Bialek, 2017; Magnasco et al., 2009). Critical dynamics show highly varying responses to

perturbations (Cocchi et al., 2017) and give rise to scale-free power spectra, scale-free avalanche  
50 statistics and long-range temporal correlations (Beggs & Timme, 2012; Chialvo, 2010). Criti-  
cality has many theoretically appealing properties, including optimized detection (Kinouchi &  
Copelli, 2006; Shew et al., 2009) and transformation (Beggs & Plenz, 2003, 2004) of sensory  
input.

Collectively, these theoretical frameworks underpin a translational literature that seeks to  
55 explain the nature of brain function (Breakspear, 2017; He, 2014) and dysfunction (Voytek &  
Knight, 2015; Zimmern, 2020). Studies within this literature tend to associate healthy brain  
activity with optimally structured emergent phenomena, including low-dimensional dynamics  
(Saggar et al., 2018), scale-free statistics (Voytek et al., 2015), and neural criticality (Ezaki  
et al., 2020). Similarly, they tend to associate deviations from this optimality with clinically  
60 relevant changes in brain activity, including disrupted neuronal excitability (Ponce-Alvarez et  
al., 2018), loss of consciousness (Solovey et al., 2015), and seizures (Maturana et al., 2020).

However, despite this large and growing body of existing literature, the function and im-  
portance of many emergent neural phenomena remains contested or controversial (Beggs &  
Timme, 2012; Destexhe & Touboul, 2021; Stumpf & Porter, 2012). For example, there is a  
65 lack of experimental evidence that reconciles weakly stable dynamics and scale-free statistics  
with stable and scale-specific circuit mechanisms of cognition or behavior (Jonas & Kording,  
2017; Krakauer et al., 2017). In contrast, most support for these and other emergent phe-  
nomena comes in three main forms. First, many studies confirm these phenomena against  
weak null models, typically generated with naive shuffling of empirical data. Such tests do not  
70 generally constitute strong evidence of function or importance (Clauset et al., 2009; Stumpf  
& Porter, 2012). Second, many studies report correlations between emergent phenomena and  
aspects of brain function (Beggs & Plenz, 2003; He et al., 2010; Solovey et al., 2015). These  
studies are interesting, but often do not fully account for confounding explanations. Third,  
many studies explain the origin or nature of emergent phenomena in computational models  
75 (Bedard et al., 2006; Chaudhuri et al., 2018; Haimovici et al., 2013; Touboul & Destexhe,  
2017). These studies, while also interesting, often require additional generative assumptions  
that can be difficult to validate. Collectively, the combined presence of strong claims about

the nature or importance of emergent neural phenomena, and the absence of similarly strong supporting evidence for these claims, has resulted in an extensive literature of intriguing but inconclusive findings.

Here, we make major steps to resolve this impasse by advancing the approach of surrogate data. This approach evaluates phenomena of interest in model datasets constrained by predefined empirical features, and is increasingly adopted to evaluate features of brain network or population activity (Elsayed & Cunningham, 2017; Rubinov, 2016). The approach has several important strengths. First, in contrast to tests against weak null models, it admits strong competing explanations. Second, in contrast to correlational studies, it closely controls for confounds by *a priori* constraining only a predefined set of features. Finally, in contrast to computational modeling studies, it makes no mechanistic assumptions, beyond assuming the importance of constrained features.

In contrast to these strengths, computational cost is a major weakness of this approach. More specifically, the generation of highly constrained model data in large recordings can often be prohibitively slow. Here, we overcame this problem by developing a fast and unbiased method for generating model data with a range of interpretable empirical features. In long neurophysiological recordings of distributed brain activity, our method outperforms standard constrained randomization (shuffling) methods by orders of magnitude. This method allowed us to rigorously evaluate emergent neural phenomena in multiregional recordings with hundreds of thousands, and in some cases millions, of timepoints across species and modalities.

We used this method to ground several major dynamical and statistical neural phenomena to time-resolved smoothness, the correlation between patterns of distributed activity at adjacent timepoints. First, we found that in electrocorticography recordings, time-resolved smoothness reliably tracked brain-state changes across consciousness and anesthesia. Second, we went beyond correlations to show that a minimal model informed by time-resolved smoothness, variance, and mean, captured major dynamical and statistical emergent neural phenomena across species and modalities. Finally, we showed that five alternative models of the neurophysiological signal, including models with many more constraints, could not explain emergent phenomena to the same extent. Collectively, our results anchor several disparately

studied emergent neural phenomena to a single and interpretable property of the neurophysiological signal. We conclude with a discussion of ways by which these results bridge theoretical frameworks with empirical observations, and thus drive progress in systems neuroscience.

## 110 **Results**

### **Summary of datasets**

Table 1 summarizes the properties of all our studied datasets. We focused our analysis and modeling on recordings with intracranial EEG modalities, namely stereotactic EEG and electroencephalography. Intracranial EEG recordings are optimally suited for the study of emergent phenomena by their combination of millimeter-scale spatial resolution, millisecond-scale temporal resolution, and distributed cortical coverage (Parvizi & Kastner, 2018). In practice, we analyzed and modeled datasets that comprised hundreds of thousands, and in some cases millions, of timepoints recorded from around 100 depth (stereotactic EEG) or grid (electrocorticography) cortical electrode channels. In addition to these recordings, we also followed the recent literature to evaluate critical emergent phenomena in light-sheet calcium imaging of fictively swimming zebrafish (Ponce-Alvarez et al., 2018). The spatiotemporal resolution of light-sheet calcium imaging data provides a unique opportunity to model brain-wide activity with cellular resolution (Ahrens et al., 2013). Nonetheless, the large number of neurons, the small number of timepoints, and the low temporal resolution of these data presented unique challenges in modeling these data, as we discuss below.

### **Time-resolved smoothness tracks conscious states**

We defined time-resolved smoothness as  $\text{corr}(\mathbf{v}_i, \mathbf{v}_{i+\text{lag}})$ , where  $\text{corr}$  denotes the Pearson correlation coefficient,  $\mathbf{v}_i$  denotes a vector of neuronal or regional activity at time  $i$ , and  $\text{lag}$  denotes an integer number of timepoints. Figure 1a-d shows the distribution of this quantity for immediately adjacent timepoints ( $\text{lag} = 1$ ), grouped separately for each species and modality. The figure shows that time-resolved smoothness was unimodally distributed close to its maximal value of 1, reflecting gradual changes in distributed brain activity over time. The medians

Table 1: Summary of analyzed and modeled datasets

Species, experiment	Modality	Nodes	Tested emergent phenomena, sampling rate	Datasets (nodes $\times$ timepoints)
Macaque monkey, anesthesia (Yanagawa et al., 2013)	Electrocorticography	Grid electrode channels covering a cortical hemisphere.	Dynamical phenomena, 1000Hz. NB: We followed previous work that established this sampling rate as a lower bound for detection of weakly stable dynamics in empirical data (Solovey et al., 2015).	128 $\times$ (3.59 million) 128 $\times$ (3.68 million) 128 $\times$ (3.69 million) 128 $\times$ (3.71 million)
Macaque monkey, resting state (Yanagawa et al., 2013)	Electrocorticography		Statistical phenomena, 250Hz. NB: All our results were robust to analysis and modeling of data at 1000Hz, but this higher sampling rate incurred unnecessary computational cost.	128 $\times$ (225 thousand) 128 $\times$ (225 thousand) 128 $\times$ (225 thousand) 128 $\times$ (225 thousand)
Humans, working memory task (Johnson et al., 2018)	Intracranial EEG: Electrocorticography and/or stereotactic EEG	Grid and/or depth electrode channels covering parts of frontal and temporal cortex.		84 $\times$ (225 thousand) 110 $\times$ (191 thousand) 106 $\times$ (210 thousand) 126 $\times$ (204 thousand)
Humans, resting-state (Goodale et al., 2020)	Stereotactic EEG	Depth electrode channels covering diverse cortical regions.		148 $\times$ (225 thousand) 157 $\times$ (225 thousand) 166 $\times$ (225 thousand) 186 $\times$ (225 thousand)
Zebrafish, fictive swimming (Mu et al., 2019)	Light-sheet calcium imaging	Neurons distributed over the whole brain.	Some statistical phenomena, 3Hz. NB: We followed previous work to adopt a modified avalanche detection procedure most suitable for analysis of brain-wide light-sheet calcium imaging data (Ponce-Alvarez et al., 2018).	(110 thousand) $\times$ 7100 (117 thousand) $\times$ 5200

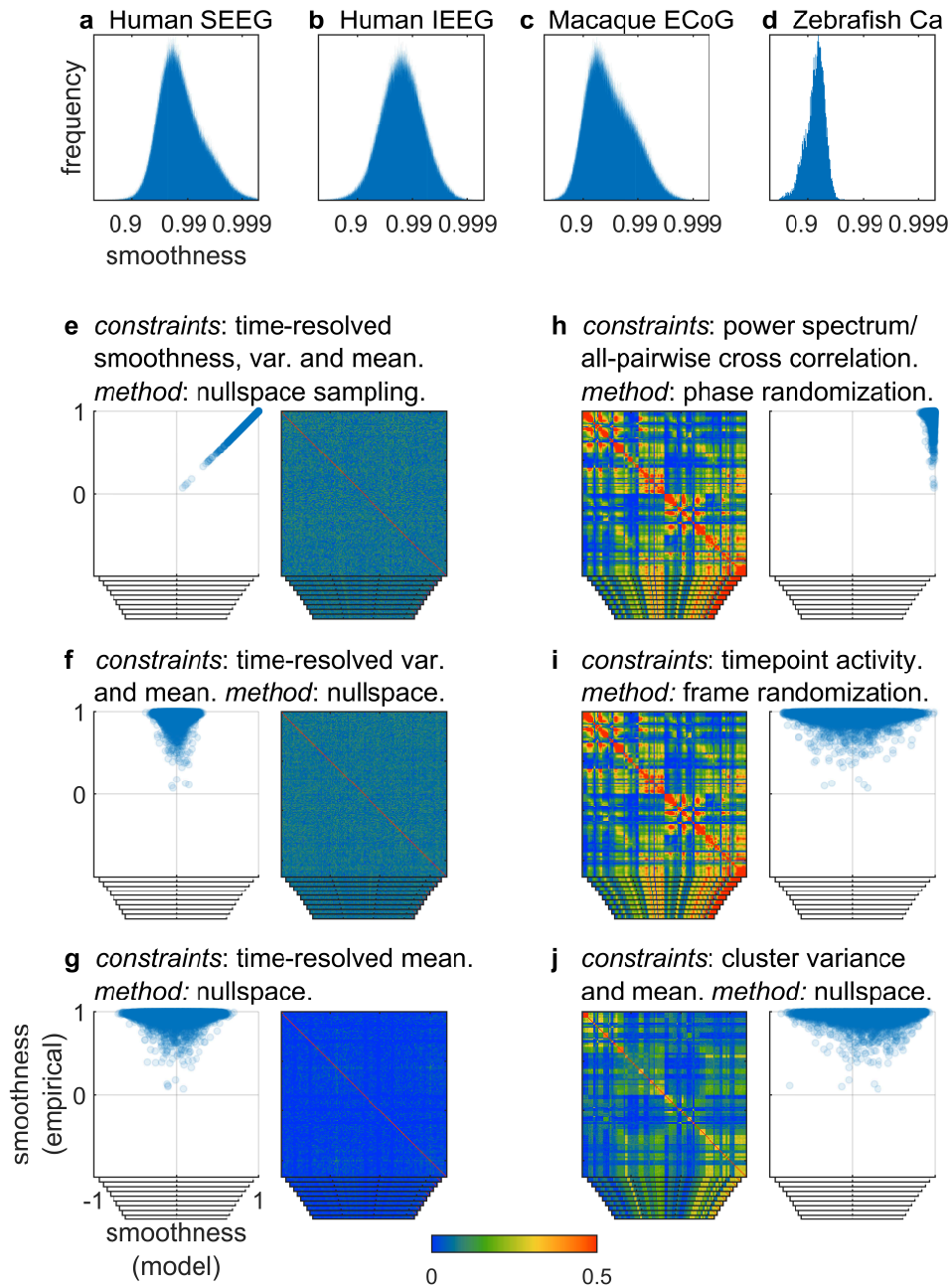


Figure 1: (a-d). Histograms of time-resolved smoothness pooled across all recordings, separately for each species and modality. Note the logarithmic x-axes. Supplementary Figures 1-4 show the relationship of time-resolved smoothness to other basic properties of the neurophysiological signal for individual modalities. (e-j) Properties of (e) *smoothness*, (f) *varmean*, (g) *mean*, (h) *power spectrum*, (i) *shuffled frames*, and (j) *varmean clusters* model data of a single representative recording (human stereotactic EEG). Scatter plots show the correspondence between empirical and model time-resolved smoothness. By definition, this correspondence is exact for *smoothness* model data. Matrices show all-pairwise node correlations. By definition, these matrices match empirical correlations exactly for *power-spectrum* and *shuffled-frames* model data. Abbreviations: SEEG, stereotactic EEG; IEEG, intracranial EEG; ECoG, electrocorticography; Ca, calcium imaging.

[90% uncertainty intervals] of this quantity were similar for all intracranial EEG modalities. They were 0.985 [0.953, 0.998] for human stereotactic EEG; 0.985 [0.936, 0.996] for human intracranial EEG; 0.964 [0.875, 0.994] for macaque electrocorticography resting-state (sampled at 250Hz), and 0.988 [0.957, 0.996] for macaque anesthesia (sampled at 1000Hz). The values were somewhat lower, 0.930 [0.845, 0.958], for zebrafish calcium imaging (sampled at 3Hz). Supplementary Figures 1-4 show the relationship of time-resolved smoothness and basic properties of the neurophysiological signal.

We adopted the approach of surrogate data to evaluate six empirically constrained models of dynamical and statistical emergent phenomena. The principles of this approach are simple. First, we defined, separately for each model, a set of empirical features, such as time-resolved smoothness or the regional power spectrum. Second, we generated ensembles of model datasets that matched the values of these features, but that were otherwise maximally random. Third, we evaluated the presence of dynamical and statistical emergent phenomena in empirical and model datasets.

The approach of surrogate data can be prohibitively slow for nontrivial constraints in large datasets. Here, we used insights from linear algebra to develop an unbiased and efficient *nullspace sampling* method for generating model timeseries with a range of interpretable constraints.

The Methods section describes our method in considerable detail. We adopted this method, alongside more standard phase and frame randomization methods (Beggs & Plenz, 2003; Prichard & Theiler, 1994), to define six competing models of the neurophysiological signal. For convenience, we refer to each model using an *italicized shorthand*. Below, we summarize the properties of each model. We also list the number of model constraints in terms of the number of nodes  $n$ , the number of timepoints  $t$ , and the percentage of total data elements.

### **Model data generated using the nullspace sampling method**

1. *smoothness*:  $3t$  ( $\sim 3\%$ ) constraints. Model data constrained by lag = 1 smoothness, variance, and mean of distributed activity at each timepoint. This was the only model that recapitulated all our considered dynamical and statistical neural emergent phenom-

160 ena across datasets. A modified version of this model with  $12t$  ( $\sim\%0.01$ ) constraints was used to model zebrafish calcium imaging data, as discussed below.

2. *varmean*:  $2t$  ( $\sim\%2$ ) constraints. Model data constrained by the variance and mean of distributed activity at each timepoint. This model allowed us to isolate the contribution of time-resolved smoothness relative to more basic properties of the neurophysiological signal.

3. *mean*:  $t$  ( $\sim\%1$ ) constraints. Model data constrained by the mean of distributed activity at each timepoint. This model represents a commonly used weak null model of the neurophysiological signal.

4. *varmean clusters*: approximately  $t$  ( $\sim\%1$ ) constraints. Model data constrained by the variance and mean of distributed activity within spatiotemporal clusters. This model denotes a basic low-dimensional representation of the data. A modified version of this model with  $8t$  ( $\sim\%0.008$ ) constraints was used to model zebrafish calcium imaging data, as discussed below.

### Model data generated using phase or frame randomization methods

175 5. *power spectrum*: more than  $\frac{1}{2}nt$  ( $\%50$ ) constraints. Model data constrained by the power spectrum of each node, and by all-pairwise node cross-correlations. This highly constrained model is often used to evaluate the presence of dynamic correlations in the neuroimaging literature (Liegeois et al., 2017). We found that, in spite of its many constraints, this model did not recapitulate all evaluated emergent phenomena across datasets.

180 6. *shuffled frames*: more than  $nt$  ( $\%100$ ) constraints. Model data constrained by shuffling of individual time frames. This model preserves the exact distributed activity of each timepoint, as well as all-pairwise node correlations.

Figure 1e-j illustrates the extent with which these models captured empirical time-resolved smoothness, as well as all-pairwise node correlations, in a representative recording. This figure allows us to make two important observations. First, it shows that *smoothness* model data (Figure 1e) does not capture node correlations, in contrast to *power-spectrum* and *shuffled-*

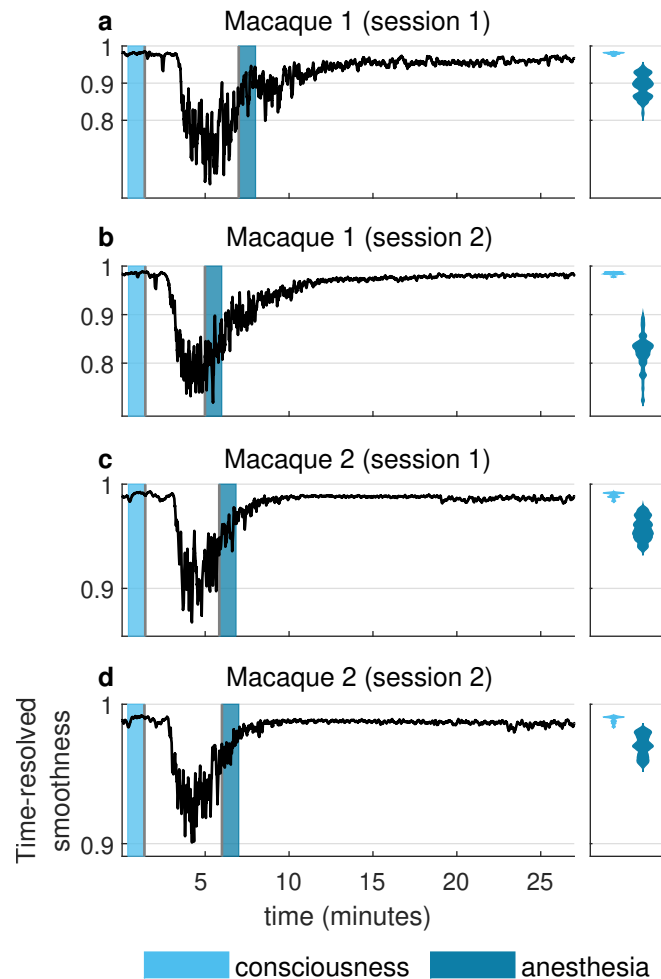


Figure 2: Changes in time-resolved smoothness track changes between consciousness and propofol anesthesia across two electrocorticography recordings of two monkeys (a-d). (Left) Light blue intervals denote a one-minute interval immediately prior to injection of propofol. Dark blue intervals denote one-minute periods immediately following onset of anesthesia based on video observation. (Right) Violin plots of time-resolved smoothness densities within shaded light-blue and dark-blue periods.

*frames* model data (Figure 1h-i). Pairwise node correlations reflect, indirectly, mechanistic network interactions that underpin cognition and behavior (S. Palva & Palva, 2012). Second, it shows that no model data, apart from *smoothness* model data, captured empirical time-  
190 resolved smoothness. These observations imply that time-resolved smoothness reflects spatially nonspecific changes of brain activity, and that these changes are distinct from spatially specific network mechanisms.

To further interpret these changes, we examined the dynamics of time-resolved smoothness in four electrocorticography recordings of macaque monkeys across consciousness and propofol anesthesia (Nagasaka et al., 2011). Previous work has shown that emergent properties  
195 of brain activity, including slope of the  $1/f$  power spectrum (Colombo et al., 2019; Gao et al., 2017; Lendner et al., 2020), as well as dynamical stability (Alonso et al., 2019; Solovey et al., 2015), separated consciousness and anesthesia in these recordings. Figure 2a-d shows that time-resolved smoothness, a simpler and decidedly non scale-free property (Figure 1a-d)  
200 likewise robustly tracked changes in consciousness across all four recordings. The median [90% uncertainty interval] time-resolved smoothness pooled over the four recordings was 0.987 [0.978, 0.992] in the one-minute interval preceding injection of propofol, and 0.939 [0.788, 0.976] in the one-minute interval immediately following the onset of anesthesia based on video observation (Solovey et al., 2015) ( $p < 10^{-10}$ , Wilcoxon rank sum test). Indeed,  
205 this metric dropped to even lower values at the peak effect time of propofol, roughly two minutes after injection (Schnider et al., 1999). Finally, the smaller relative drop of time-resolved smoothness in macaque 2 (Figure 2c-d) matched previous observations that this monkey was not fully anesthetized (Alonso et al., 2019). Collectively, these results show that time-resolved smoothness can robustly track gross changes in brain activity across conscious states.

## 210 **Time-resolved smoothness is sufficient to explain emergent dynamics**

An important advantage of our approach is the ability to go beyond correlations and evaluate the sufficiency of basic constraints to explain emergent phenomena. We first evaluated the sufficiency of model data to explain dynamical stability, an emergent dynamical phenomenon (Deco et al., 2011). We followed previous work to estimate dynamical stability using the eigen-

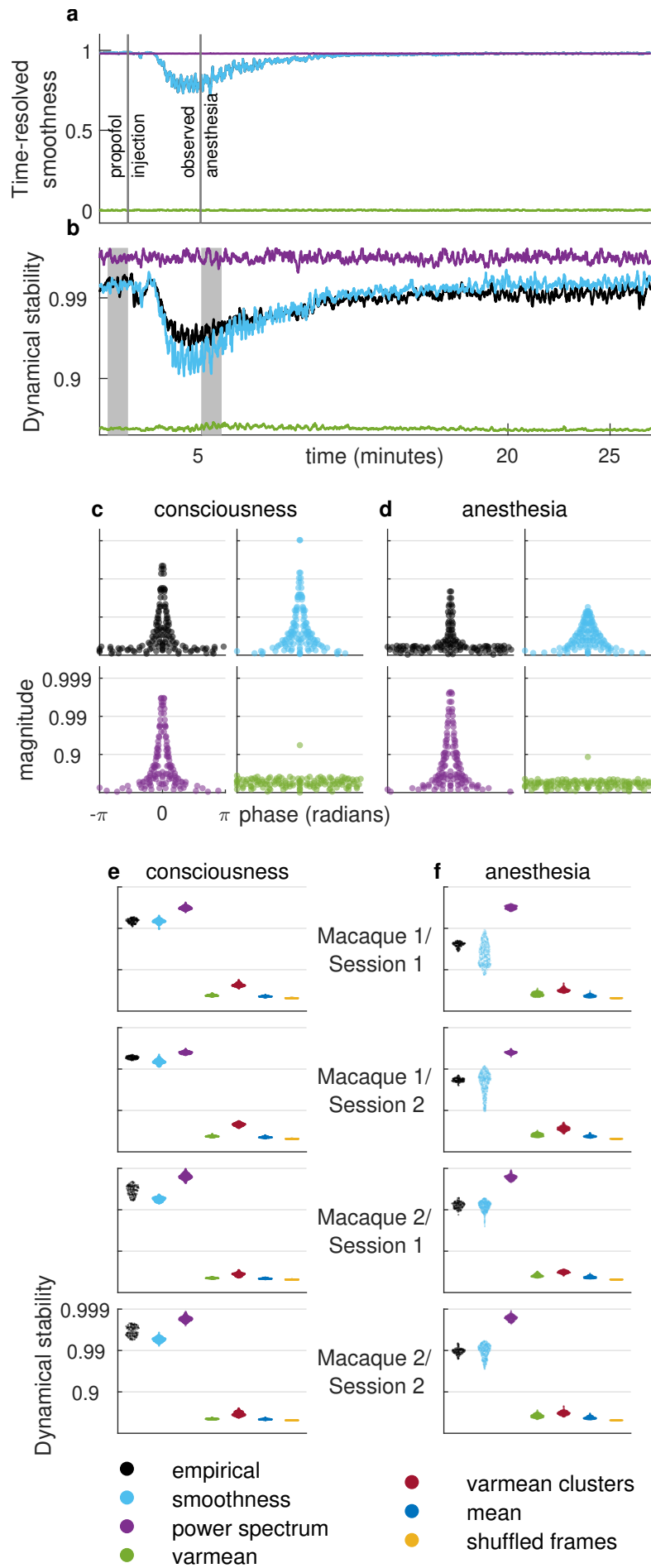


Figure 3: See caption on next page.

Figure 3: Time-resolved smoothness explains changes in dynamical stability across consciousness and propofol anesthesia. (a) Fluctuations of time-resolved smoothness for *smoothness*, *power-spectrum* and *varmean* model data in a representative electrocorticography recording. (b) Dynamical stability index, the median value of the 5% largest eigenvalues, for the same recording. Note the strong correlation of time-resolved smoothness with dynamical stability. (c-d) Phase and magnitude of eigenvalues of a vector autoregressive model fit to a single window from periods of consciousness and anesthesia (shaded intervals in panel (b), equivalent to intervals in Figure 2). Note the drop of dynamical stability in anesthesia in empirical data, as well as in *smoothness* model data. (e-f) Dynamical stability index across all empirical and model data, pooled over all recordings and averaged over all windows denoting periods of consciousness and anesthesia. Results on model data were derived from 50 samples for each model of each dataset. Supplementary Figures 5-8 show individual results for all empirical and model datasets.

215 value spectrum of a time-resolved vector autoregressive model (Magnasco et al., 2009; Solovey et al., 2015; Solovey et al., 2012), a locally linear approximation of distributed brain activity. Theory predicts that interesting, weakly stable dynamics have largest eigenvalues with magnitudes that approach 1. Conversely, less interesting, strongly stable dynamics have largest eigenvalues with smaller magnitudes. Previous stability analyses of monkey electrocorticogra-  
 220 phy recordings found that consciousness associates with weakly stable dynamics, and propofol anesthesia associates with strongly stable dynamics (Alonso et al., 2014; Alonso et al., 2019; Solovey et al., 2015).

Figure 3a-c shows that the *smoothness* model, and no other evaluated models, reproduced empirical changes in dynamical stability across consciousness and propofol anesthesia. We  
 225 quantified dynamical stability by the median magnitude of the 5% largest eigenvalues. Stability estimates pooled across four empirical recordings showed that this index had a median [90% uncertainty interval] of 0.995 [0.992, 0.998] during an interval of consciousness, and 0.985 [0.972, 0.993] during an interval of anesthesia ( $p < 10^{-10}$ , Wilcoxon rank sum test). Similarly, the stability of *smoothness* model data was 0.994 [0.992, 0.995] during conscious-  
 230 ness, and 0.986 [0.920, 0.994] during anesthesia ( $p < 10^{-10}$ ). In contrast, *power-spectrum* model data showed weakly stable dynamics (0.997 [0.996, 0.999]) during consciousness but no change in stability (0.998 [0.996, 0.999]) during anesthesia ( $p = 0.243$ ). All other model data showed strongly stable dynamics across consciousness and anesthesia (Figure 3e-f, Supplementary Figures 5-8).

## 235 **Time-resolved smoothness is sufficient to explain scale-free statistics**

We next evaluated the extent with which model data accounted for scale-free statistical phenomena. We considered two commonly studied signatures of these phenomena:  $1/f$  power-frequency relationships and long-range temporal correlations.  $1/f$  denotes the decay of spectral power as a function of frequency. This scale-free, or arrhythmic, power-frequency relationship is distinct from neuronal oscillations, which represent narrow peaks in frequency spectra. This relationship is typically represented by the slope of the  $1/f$  power spectrum.

Figure 4a-c, and Supplementary Figures 9-19, show that, inline with previous observations (He et al., 2010; Peterson et al., 2017; Voytek et al., 2015), we found robust  $1/f$  scaling of spectral power in a broad 1 to 80Hz frequency range. Specifically, we found that empirical data across all intracranial EEG recordings showed a mean [90% uncertainty interval] exponent values of 2.834 [1.827, 3.989]. Notably, *smoothness* model data likewise showed prominent  $1/f$  scaling with exponents 2.071 [1.869, 2.639] across all intracranial EEG recordings. The values of these exponents were necessarily more uniform because the model is spatially agnostic by definition. Nevertheless, these values were inline with empirical values ( $p = 0.170$  that any model exponent was at least equal to any empirical exponent). Notably, no other model data, with the trivial exception of the *power-spectrum* model data, showed  $1/f$  scaling.

We next considered long-range temporal correlations, emergent phenomena that track the statistical self-similarity of long timeseries. Typically, these correlations are defined by the scaling exponent of mean fluctuations in the amplitude envelope in alpha or beta frequency bands, using detrended fluctuation analysis, a method especially applicable to nonstationary timeseries (Peng et al., 1995). The scaling exponent between window sizes and mean fluctuations indexes the presence of statistical self-similarity. Values of this exponent considerably larger than 0.5 denote interesting, self-similar (fractal-like) structure. In contrast, values close to 0.5 denote less interesting, random (white-noise-like) structure (Linkenkaer-Hansen et al., 2001).

Figure 4d-f, and Supplementary Figures 9-19, show robust power-law scaling for mean fluctuations in amplitude for all empirical datasets in the alpha frequency band (results were similar for the beta frequency band, not shown). The scaling exponents for empirical datasets

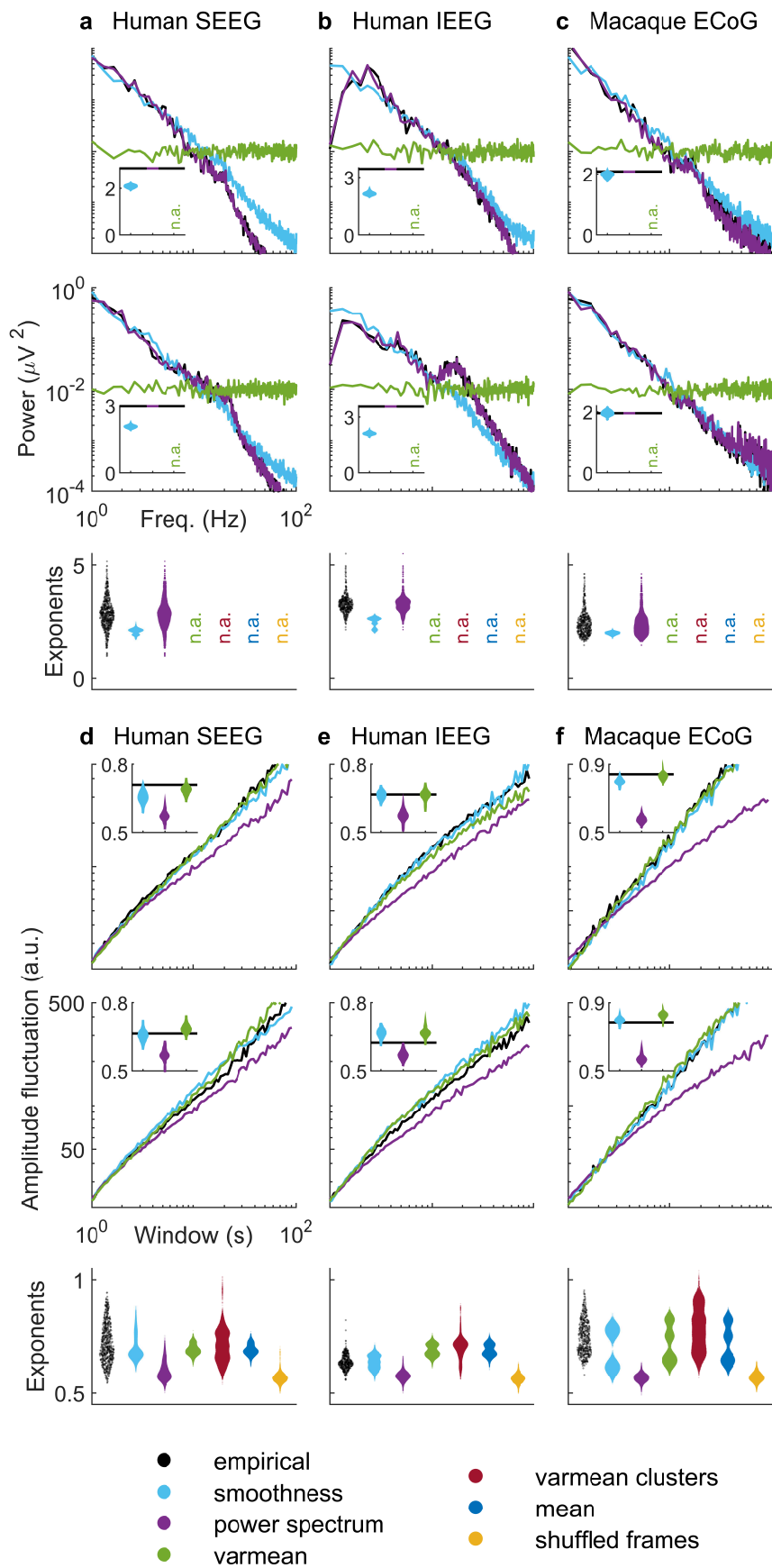


Figure 4: See caption on next page.

Figure 4: Time-resolved smoothness explains empirical  $1/f$  scaling and long-range temporal correlations. (a-c) Top two panels show  $1/f$  scaling of spectral power as a function of frequency for two channels of representative intracranial EEG recordings. Insets show violin plots of  $1/f$  slope exponents benchmarked against empirical exponents (solid black lines). Bottom panels show violin plots of exponents pooled across all channels and all empirical and model datasets. n.a. denotes lack of power-law fit. (d-e) Top panels show scaling of time-resolved amplitude as a function of window for two representative channels. Insets show violin plots of scaling exponents, benchmarked against empirical exponents (solid black lines). Bottom panels show violin plots of all exponents pooled across all channels and all empirical and model datasets. Results on model data were derived from 50 samples for each model of each dataset. Supplementary Figures 9-19 show individual results for all empirical and model datasets. Abbreviations: SEEG, stereotactic EEG; IEEG, intracranial EEG; ECoG, electrocorticography; Ca, calcium imaging.

were within the range previously reported in literature. Specifically, we found that empirical  
265 recordings across all intracranial EEG modalities showed a median [90% uncertainty interval]  
exponent values of 0.687 [0.599, 0.868]. *Smoothness* model data showed similar exponents  
across all intracranial EEG recordings (0.666 [0.594, 0.800],  $p = 0.409$ ). In contrast, *power-*  
*spectrum* model data showed exponents that were considerably closer to white-noise values  
(0.576 [0.543, 0.646]), and that significantly deviated from values of empirical exponents ( $p =$   
270 0.048). Collectively, these findings indicate that only the *smoothness* model data exhibited  
both  $1/f$  scaling and long-range temporal correlations across datasets.

## **Time-resolved smoothness is sufficient to explain avalanche statistics**

Neural avalanches are transient periods of coordinated activity between groups of neurons or  
brain regions. The study of avalanche dynamics plays a prominent role in the theory of neural  
275 criticality. One commonly studied phenomenon in this literature is the power-law scaling of  
avalanche size and duration distributions. Nonetheless, studies have also emphasized that  
this scaling may not be strongly indicative of critical dynamics (Touboul & Destexhe, 2010),  
and recent work has focused on more specific signatures of criticality, including power-law  
relationships between size and duration exponents (Friedman et al., 2012), as well as shape  
280 collapse, a universal scaling relationship of avalanche phase with activity (Friedman et al.,  
2012; Ponce-Alvarez et al., 2018; Sethna et al., 2001). Shape collapse, in particular, is a strict  
criterion of neural criticality, obtained through averaging hundreds or thousands of individual

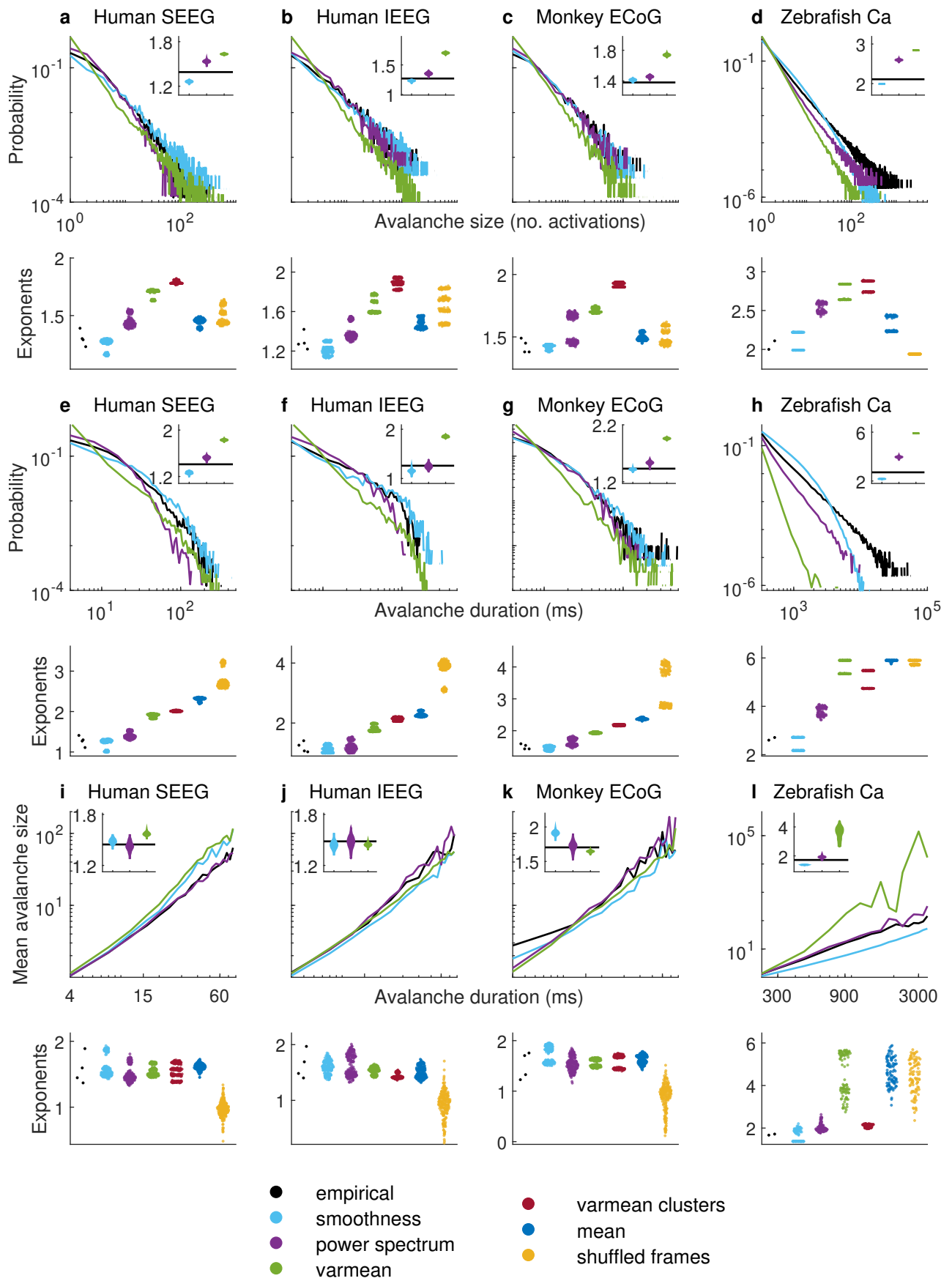


Figure 5: See caption on next page.

Figure 5: Time-resolved smoothness explains avalanche statistics. (a-d) Avalanche size probability distributions. (e-h) Avalanche duration probability distributions. (i-l) Scaling of avalanche size and duration exponents. Inset violin plots show normalized distributions of model exponents, benchmarked against empirical exponents (solid black lines). Bottom panels show violin plots of all empirical and model exponents pooled across all empirical and model datasets. Results on model data were derived from 50 samples for each model of each dataset. Supplementary Figures 20-32 show individual results for all empirical and model datasets. Abbreviations: SEEG, stereotactic EEG; IEEG, intracranial EEG; ECoG, electrocorticography; Ca, calcium imaging.

avalanches. Theory predicts that at criticality, collapsed temporal profiles of avalanches will converge to a universal shape independent of avalanche duration (Beggs & Timme, 2012; Friedman et al., 2012; Sethna et al., 2001).

We first evaluated the presence of avalanche phenomena in all intracranial EEG datasets. Figure 5, and Supplementary Figures 20-30, show robust signatures of power-law scaling for avalanche sizes, durations, and size-duration relationships. Specifically, across all intracranial EEG datasets, avalanche sizes decayed with a median [90% uncertainty interval] power-law exponents of 1.340 [1.221, 1.486]. Correspondingly, avalanche durations decayed with an exponent of 1.355 [1.043, 1.585]. Finally, avalanche sizes scaled as a function of avalanche durations with exponents of 1.539 [1.237, 1.960]. *Smoothness* model data largely recapitulated these signatures with exponents of 1.285 [1.150, 1.430] ( $p = 0.260$ ) for avalanche sizes, 1.280 [1.000, 1.520] ( $p = 0.384$ ) for avalanche durations, and 1.584 [1.444, 1.906] ( $p = 0.606$ ) for scaling of size as a function of duration. In contrast, all other model data, except *power-spectrum* model data, had a considerable number of exponents that significantly deviated from empirical values (Figure 5).

Figure 6, and Supplementary Figures 20-30, show that empirical data exhibited avalanche shape collapses indicative of universal scaling. Notably, *smoothness*, *power-spectrum*, and *varmean* model data all had similar shape collapses. The mean avalanche temporal profiles in these model data all peaked at similar times. Indeed, the variance between rescaled avalanche shapes had a median [90% uncertainty interval] of 0.098 [0.037, 0.299] for empirical data, 0.088 [0.043, 0.349] ( $p = 0.507$ ) for *smoothness* model data, 0.080 [0.043, 0.204] ( $p = 0.558$ ) for *power-spectrum* model data, and 0.120 [0.055, 0.419] ( $p = 0.383$ ) for *varmean* model

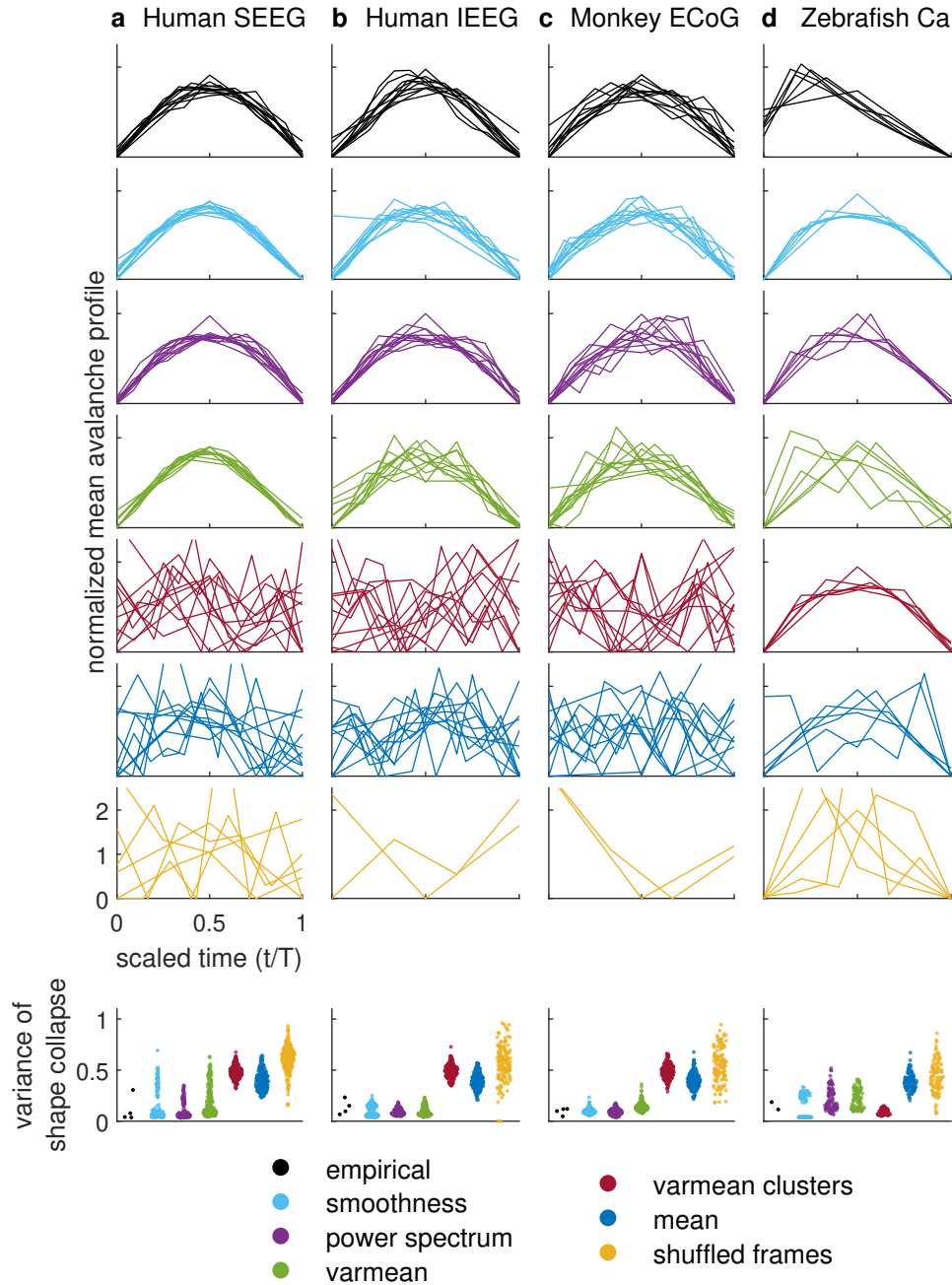


Figure 6: Model data constrained by time-resolved features, but not other properties of data, pass stringent tests of criticality. (a-d) Shape collapses: scaling of mean temporal profiles with avalanche activity. Bottom panels show violin plots of all empirical and model variance between avalanche scaling profiles (lower is better). Results on model data were derived from 50 samples for each model of each dataset. Supplementary Figures 20-32 show individual results for all empirical and model datasets. Abbreviations: SEEG, stereotactic EEG; IEEG, intracranial EEG; ECoG, electrocorticography; Ca, calcium imaging.

305 data. All other models lacked universal shape collapses. These results imply that basic time-resolved constraints are sufficient to generate data that pass stringent tests of criticality.

## **Time-resolved smoothness of brain-wide calcium imaging data**

Finally, we sought to evaluate emergent phenomena in calcium imaging recordings of fictively swimming zebrafish. These data provide an unmatched spatiotemporal resolution of brain-wide cellular activity (Ahrens et al., 2013). At the same time, the distinct nature of these data present several methodological challenges (Table 1). Specifically, in contrast to intracranial EEG recordings, brain-wide calcium imaging recordings were imaged at a relatively low frequency (about 3Hz), had many more nodes (about 100 thousand neurons), and many fewer timepoints (about 6 thousand). The low sampling rate limited our evaluation to critical emergent phenomena, inline with recent work (Ponce-Alvarez et al., 2018). The large number of nodes imposed memory requirements which precluded the use of nullspace sampling and required the adoption of memory efficient but slow constrained randomization methods (El-sayed & Cunningham, 2017; Rubinov, 2016). Moreover, low-frequency imaging resulted in considerably lower values of time-resolved smoothness (Figure 1d). We compensated for this drop in smoothness by constraining time-resolved smoothness between a single frame and its four adjacent neighbors. Similarly, the distinct dimensionality of these data resulted in *varmean-clusters* models that had substantially more constraints. Finally, standard avalanche-detection methods in these data result in a trivial detection of a single never-ending brain-wide avalanche. We compensated for this problem by adopting a spatially contiguous definition of avalanches (Ponce-Alvarez et al., 2018), which in turn penalizes spatially agnostic models, such as the *smoothness* model.

These caveats aside, our modeling results on these datasets were generally inline with results on intracranial EEG data. Figure 6, and Supplementary Figures 31-32 show that empirical calcium-imaging avalanche sizes decayed as power laws with exponents 2.110 and 2.000, avalanche durations decayed as power laws with exponents 2.710 and 2.600, and avalanche sizes scaled as a function of durations with power-law exponents of 1.717 and 1.667. *Smoothness* model data had similar median [90% uncertainty interval] values of these exponents.

Specifically, it had avalanche size exponents of 2.105 [1.999, 2.220], duration exponents of 2.445 [2.160, 2.720], and size-duration scaling exponents of 1.523 [1.374, 2.038] (we do not report  $p$  values because we only have two observations of empirical exponents). The exponents of most other models deviated to a larger extent from those values, while shape collapse results were largely inline with those observed on intracranial EEG datasets (see Figure 6, and Supplementary Figures 31-32 for a summary of all results).

## Discussion

A major aim of systems neuroscience is to understand how collective neural interactions give rise to brain function. A burgeoning literature in the field has proposed, over the last two decades, that several emergent neural phenomena enable the emergence of such function. The growth of this literature, however, has not been matched by a corresponding growth in conceptual and methodological advances for reconciling high-level neural phenomena with known properties of the neurophysiological signal. One key hurdle for such advances has been the difficulty in scaling methods of surrogate data to long multiregional recordings.

Here, we developed a new method to generate surrogate data constrained by interpretable empirical properties in multivariate timeseries with hundreds of thousands, and even millions, of timepoints (Table 1). This method allowed us to rigorously ground, for the first time, several prominent emergent neural phenomena to an interpretable property of the neurophysiological signal. Our main results (Figures 3-6) show that empirical constraints of time-resolved smoothness, variance, and mean, recapitulated all evaluated emergent phenomena across modalities and species. Importantly, a model informed by these constraints outperformed competing models with many more constraints, including models informed by full power spectra and cross-correlation structure.

The nature of time-resolved smoothness offers strong clues to the nature of our evaluated phenomena. Notably, this metric is agnostic to properties of individual nodes (regions or cells), and therefore cannot, by definition, capture mechanistic network interactions. Figure 1 illustrates this effect as the lack of correlation structure for timeseries constrained by time-resolved smoothness. Put another way, knowledge of time-resolved smoothness tells us little

about how specific network elements interact to cause brain function. Importantly, this does not imply that past discoveries of emergent neural phenomena are false. On the contrary, we were able to robustly replicate these discoveries across modalities. Instead, this implies that, by the principle of scientific parsimony (Occam's razor), it may be needlessly complicated to  
365 imbue emergent neural phenomena with function that transcends properties of time-resolved smoothness.

What then is the relevance of emergent neural phenomena for brain function? Our results offer one plausible answer by closely linking time-resolved smoothness to global changes of distributed brain activity during propofol anesthesia (Figure 2). We hypothesize that more  
370 subtle changes of time-resolved smoothness, and the accompanying emergent phenomena, will likewise track subtle neuromodulatory changes associated with sensory, cognitive, and motor function (Bargmann, 2012; Marder, 2012). Indeed, it may be possible to test this falsifiable hypothesis with future high-speed multicellular imaging data that can capture subtle changes in distributed activity across brain states (Demas et al., 2021; Stringer et al., 2019).

375 More generally, our results offer to unify and simplify existing theoretical frameworks in systems neuroscience in several ways. First, these results provide a roadmap for future neurobiological explanations of emergent phenomena. Specifically, we propose that the discovery of molecular, cellular or circuit mechanisms of time-resolved smoothness will lead to the corresponding discovery of mechanisms that underpin a range of emergent phenomena.  
380 Prime targets for such mechanisms include the action of widely projecting subcortical systems that modulate cortical excitability and arousal (Avery & Krichmar, 2017; Jones, 2005; Lee & Dan, 2012). Second, our results provide a new perspective on regional variation of scale-free activity (Gao et al., 2017; He et al., 2010; Lendner et al., 2020). This variation is related, although not equivalent, to the notion of hierarchy of cortical timescales (Chaudhuri et al.,  
385 2015; Gao et al., 2020; Honey et al., 2012; Murray et al., 2014; Raut et al., 2021). Our results clarify the meaning of this regional variation by noting that time-resolved smoothness of distributed interactions can automatically give rise to scale-free activity. This finding suggests that scale-free regional variation can be more intuitively interpreted as the extent of regional contribution to changes in distributed activity, and without need to explain high-level scale-

390 free phenomena. Third, our results have considerable implications for a growing translational literature that centers on the study of emergent phenomena (Voytek & Knight, 2015; Zimmern, 2020). Much of this literature seeks to find alterations in distinct emergent neural phenomena across healthy and diseased brain states (Maturana et al., 2020; Ponce-Alvarez et al., 2018; Solovey et al., 2015). Our findings show that a single interpretable property of the neurophysi-  
395 ological signal can replace, in this literature, a battery of high-level clinical biomarkers. In this way, our findings can accelerate translation by motivating future discovery of mechanisms that affect time-resolved smoothness across clinical states.

Finally, we stress that our discovery was ultimately made possible by the development of a new method to generate surrogate data of long multiregional recordings (Elsayed & Cun-  
400 ningham, 2017; Rubinov, 2016). As systems neuroscientists come against bigger and more highly resolved neurophysiological datasets, the development of scalable modeling methods will become increasingly important for rigorous analysis and modeling of these data. Indeed, we hope that future adoption of our method will allow investigators to comprehensively evaluate other aspects of multiregional recordings across brain states. Ultimately, we consider  
405 that widespread adoption of this and similar methods will be necessary to enable unified and cohesive explanations of distributed brain structure and activity.

# Methods

## Generation of empirically constrained model data

### Definition of time-resolved smoothness

We defined time-resolved smoothness as,

$$\text{smoothness}_{i,\text{lag}} = \frac{\sum_{j=1}^n (\mathbf{v}_i^j - \bar{\mathbf{v}}_i)(\mathbf{v}_{i+\text{lag}}^j - \bar{\mathbf{v}}_{i+\text{lag}})}{\sqrt{\sum_{j=1}^n (\mathbf{v}_i^j - \bar{\mathbf{v}}_i) \sum_{j=1}^n (\mathbf{v}_{i+\text{lag}}^j - \bar{\mathbf{v}}_{i+\text{lag}})}}.$$

410 where  $\mathbf{v}_i^j$  denotes the activity of node  $j$  at time  $i$ ,  $\bar{\mathbf{v}}_i$  denotes the mean activity of all nodes at time  $i$ , and lag is an integer.

It is easy to show that average time-resolved smoothness is related to average node autocorrelation as follows,

$$\begin{pmatrix} \text{time-resolved smoothness} \\ \text{averaged over all timepoints} \end{pmatrix} \approx \begin{pmatrix} \text{node autocorrelation} \\ \text{averaged over all nodes} \end{pmatrix} \quad (1)$$

This equivalence holds because both quantities in equation 1 represent averaged dot products, normalized either over the activity of all nodes at a single timepoint (time-resolved smoothness), or over the activity of a single node at all timepoints (node autocorrelation). At the same  
415 time, the non-averaged versions of these quantities are incommensurate because time-resolved smoothness is defined for each timepoint, while autocorrelation is defined for each node.

### General formulation of nullspace sampling

Our sampling method expresses empirical features of interest as sets of linear equations. Formally, let us define  $\mathbf{v} \in \mathcal{R}^{n \times t}$  to be the empirical timeseries of  $n$  nodes and  $t$  timepoints. Let  
420 us also define  $\text{vec}(\cdot)$  to be a vectorization or flattening operator, such that  $\text{vec}(\mathbf{v}) \in \mathcal{R}^{nt \times 1}$ .

Let us now consider  $m$  features of interest, define  $\mathbf{b} \in \mathcal{R}^{m \times 1}$  to be the empirical values of these features, and define  $\mathbf{A} \in \mathcal{R}^{m \times nt}$  to represent the coefficient matrix for these features.

Formally we can write,

$$\mathbf{A} \text{vec}(\mathbf{v}) = \mathbf{b}, \quad (2)$$

Without loss of generality, let us assume that the empirical features of interest are linearly independent (and therefore that the matrix  $\mathbf{A}$  is full rank). Since the number of these features will, in most cases, be much smaller than the number of data elements ( $m \ll nt$ ), we end up with an underdetermined set of linear equations. It follows that we can generate model data by  
 425 unbiasedly sampling from the solution space of this set.

Linear algebra tells us that this solution space is spanned by orthogonal unit vectors that form the nullspace of the coefficient matrix  $\mathbf{A}$  (Laub, 2005). Let us define  $\mathbf{Z} \in \mathcal{R}^{nt \times (nt-m)}$  as this nullspace, such that  $\mathbf{AZ} = 0$ . We can then express the solution space as,

$$\text{vec}(\mathbf{x}) = \text{vec}(\mathbf{x}_0) + k\mathbf{Z}\mathbf{q} \quad (3)$$

where  $x_0$  denotes the minimum-norm solution,  $k$  is a scaling constant and  $\mathbf{q} \in \mathcal{R}^{(nt-m) \times 1}$  is a uniformly sampled random weighting vector. Geometrically, each row in  $\mathbf{A}$  represents an unbounded hyperplane in  $nt$  dimensions and the solution space is an  $nt - m$  vector space formed by the intersection of these hyperplanes.

430 We regularized the space of these solutions by constraining the Frobenius norm of all model timeseries to empirical values. We did this by first setting the norm of  $\mathbf{q}$  to 1. Uniformly sampling  $\mathbf{q}$  with  $|\mathbf{q}| = 1$  is equivalent to sampling from the surface of the  $nt - m$  dimensional hypersphere of radius 1 and centered at the origin. This sampling can be achieved by generating vectors from the  $nt - m$  dimensional standard normal distribution and rescaling  
 435 the vectors to have unit norm. This procedure guarantees to produce random samples uniformly distributed on the surface of the hypersphere (Smith, 1984). We then used the scaling parameter  $k$  to rescale the norm to match the empirical timeseries. To determine the value of  $k$ , we note that  $\text{vec}(\mathbf{x}_0) = \mathbf{A}^\dagger \mathbf{b}$  where  $\cdot^\dagger$  denotes the Moore-Penrose pseudoinverse. From the standard theorem of algebra, we know that  $\text{vec}(\mathbf{x}_0)$  is always orthogonal to  $\mathbf{Z}$ . Because the

440 two additive components in equation 3 are orthogonal, we can use Pythagoras theorem to set  $k = \sqrt{|\mathbf{v}|^2 - |\mathbf{x}_0|^2}$  and thereby ensure that the Frobenius norm of  $\mathbf{x}$  equals the norm of  $\mathbf{v}$ .

Once we set  $k$  and  $\mathbf{q}$ , we can then directly sample datasets  $\mathbf{x}$ . Because  $\mathbf{Z}$  is an orthonormal matrix, our sampling is guaranteed to be uniform as long as  $\mathbf{q}$  is drawn from a multivariate uniform distribution. We used standard MATLAB functions such as `qr` and `svd` to build orthonormal nullspaces. Once we compute the nullspace, it becomes trivial to sample  $\mathbf{q}$  from a multivariate uniform distribution and generate model timeseries. Box 1 summarizes the complete sequence of steps in the general formulation of nullspace sampling.

### Box 1. Summary of nullspace sampling

1. Define empirical features through linear equations,  $\mathbf{A} \text{vec}(\mathbf{v}) = \mathbf{b}$ .
2. Compute orthonormal nullspace matrix  $\mathbf{Z}$  of the coefficient matrix  $\mathbf{A}$ .
3. Compute the minimum-norm solution  $\text{vec}(\mathbf{x}_0)$ .
4. Uniformly sample the weighting vector  $\mathbf{q}$  and compute the scaling parameter  $k$ .
5. Generate model data using  $\text{vec}(\mathbf{x}) = \text{vec}(\mathbf{x}_0) + k\mathbf{Z}\mathbf{q}$ .

### 450 Sequential nullspace sampling with nonlinear constraints

The general formulation of nullspace sampling admits only linear constraints, and produces massive nullspace matrices of close to  $(nt)^2$  elements. This formulation is of limited use for constraining time-resolved smoothness and other nonlinear constraints in large datasets. Nonetheless, here we exploited the sequential definition of time-resolved smoothness to allow nullspace sampling with nonlinear constraints in long multiregional recordings.

We first expressed empirical timeseries  $\mathbf{v}$  as a sequence of vectors  $\mathbf{v}_1, \mathbf{v}_2, \dots, \mathbf{v}_t$ , where  $\mathbf{v}_i \in \mathcal{R}^{n \times 1}$  denotes the activity of all nodes at time  $i$ . Likewise, we expressed model timeseries  $\mathbf{x} \in \mathcal{R}^{n \times t}$  as a sequence of activity vectors  $\mathbf{x}_1, \mathbf{x}_2, \dots, \mathbf{x}_t$ , with  $\mathbf{x}_i \in \mathcal{R}^{n \times 1}$ . We then defined correlations between adjacent timepoints as  $c_1, c_2, \dots, c_{t-1}$ , where  $c_i = \mathbf{v}_i \cdot \mathbf{v}_{i+1} = \mathbf{x}_i \cdot \mathbf{x}_{i+1}$  and  $\cdot$  denotes the dot product.

This formulation allowed us to generate model timeseries with correlation constraints sequentially, timepoint by timepoint. Specifically, at each timepoint  $i$ , we used model data  $\mathbf{x}_i$  as the coefficient matrix to generate model data at timepoint  $i + 1$ . Without loss of generality, we used the following algorithm to generate  $\mathbf{x}_{i+1}$  with zero mean and unit standard deviation:

- 465 1. For  $i = 0$ , sample a random normally distributed vector  $\mathbf{x}_1$  with zero mean and unit standard deviation.
2. For  $i = 1, 2 \dots t - 1$ , sample  $\mathbf{x}_{i+1}$  by solving,

$$[\mathbf{x}_i, \mathbf{1}]^\top \mathbf{x}_{i+1} = \begin{bmatrix} c_i \\ 0 \end{bmatrix} \quad (4)$$

$$|\mathbf{x}_{i+1}| = n - 1 \quad (5)$$

where  $\mathbf{1}$  denotes the all-ones vector. The structure of the coefficient matrix in equation 4 guarantees that  $\mathbf{x}_{i+1}$  will always have zero mean, and together with equation 5 guarantees that the vector will have unit standard deviation. Model vectors can then be simply rescaled to match  
 470 the mean and standard deviation of empirical data.

In practice, this sequential generation of empirical data required nullspace matrices with approximately  $n^2$  elements, and scaled linearly with the number of timepoints  $t$ . This approach was feasible for long intracranial EEG data ( $n \approx 100$ ), where it outperformed standard constrained randomization methods (Elsayed & Cunningham, 2017; Rubinov, 2016) by orders  
 475 of magnitude. On the other, the approach was not feasible for brain-wide cellular calcium imaging datasets ( $n \approx 10^5$ ). For these data, we replaced nullspace sampling with memory-efficient but slow constrained randomization methods.

### Implementation of mean and variance constraints

In some cases (*mean*, *varmean*, and *varmean-clusters* models), we constrained model data by empirical mean and variance, but not by smoothness. In such cases, we generated  $\mathbf{x}_i$  by

solving

$$\mathbf{1}^\top \mathbf{x}_i = 0 \quad (6)$$

$$\text{with } |\mathbf{x}_i| = n - 1. \quad (7)$$

To enforce these constraints within spatiotemporal clusters (*varmean-clusters* model), we used  
 480 k-means clustering to group  $n$  nodes into spatial clusters, and separately  $t$  timepoints into  
 temporal clusters. For long multiregional recordings, we set spatial clusters to have on average  
 5 nodes, and separately temporal clusters to have an average of 50 timepoints. To prevent an  
 excessive number of clusters in brain-wide cellular calcium imaging recordings, we set spatial  
 clusters in these datasets to have an average of 250 nodes, and temporal clusters to have an  
 485 average of 100 timepoints.

To further optimize the efficiency of nullspace sampling, we derived an analytical expres-  
 sion for the nullspace  $\mathbf{Z} \in \mathcal{R}^{n \times (n-1)}$  of the coefficient matrix  $\mathbf{A} = \mathbf{1}^\top$  in equation 6,

$$\mathbf{Z} = \begin{pmatrix} -c & -c & -c & \dots & -c \\ b & -a & -a & \dots & -a \\ -a & b & -a & \dots & -a \\ -a & -a & b & \dots & -a \\ \vdots & \vdots & \vdots & \vdots & \vdots \\ -a & -a & \dots & -a & b \end{pmatrix},$$

where  $a$ ,  $b$  and  $c$  denote solutions to the following set of equations:

$$\begin{aligned} b - a(n - 2) - c &= 0 \\ c^2 + a^2(n - 2) + b^2 - 1 &= 0 \\ c^2 - 2ab + (n - 3)a^2 &= 0 \end{aligned}$$

One can directly verify that this solution is an orthonormal nullspace of the coefficient matrix  $\mathbf{A} = \mathbf{1}^\top$ , such that  $\mathbf{Z}^\top \mathbf{Z} = \mathbf{I}$  and  $\mathbf{AZ} = 0$ . In practice, this analytical formulation allowed us to eschew the use of numerical computational methods for computing the nullspace of *mean*, *varmean*, and *varmean-clusters* models.

## 490 **Phase randomization**

We generated phase-randomized model data using a well-known algorithm from the physics and neuroscience literature (Liegeois et al., 2017; Prichard & Theiler, 1994). Briefly, we first used the Fourier transform to compute the phase and amplitude of each timeseries. We then rotated the phase of all nodes at each frequency by a random complex variable  $e^{i\phi}$  with  $\phi$  uni-  
495 formly distributed in  $[-\pi, \pi]$ . Finally, we obtained model timeseries by computing the inverse Fourier transform of these phase-randomized data. This method is guaranteed to generate maximally random data that preserve nodal power spectra and full cross-correlation structure.

## **Details of data acquisition**

### **Macaque electrocorticography (Neurotycho)**

500 Data were collected at the Laboratory for Adaptive Intelligence, Brain Science Institute, RIKEN. Electrocorticography recordings were made from two male macaques before, during, and after administration of propofol anesthesia. Grid electrodes were implanted on the frontal, parietal, temporal, and occipital lobes. Additional experimental details for these data are provided in previous studies (Nagasaka et al., 2011; Yanagawa et al., 2013). These data are publicly  
505 available from <http://www.neurotycho.org>.

### **Human intracranial EEG**

Data were acquired at the University of California Irvine Hospital. Intracranial EEG recordings were made from adult epileptic patients performing a visuospatial working memory task. Grid and/or depth electrodes were implanted in frontal and medial temporal lobes. Additional  
510 experimental details for these the data are provided in a previous study (Johnson et al., 2018). These data are publicly available from <http://www.crcns.org> (Johnson, 2018).

## **Human stereotactic EEG**

Data were acquired at Vanderbilt University Medical Center. Stereotactic EEG recordings were made from adult epilepsy patients, one day after electrode implantation and before medication wean. The patients were instructed to keep their eyes closed and remain awake for  
515 twenty minutes. Depth electrodes were implanted in cortical regions, depending on suspected seizure origin. Additional experimental details for these data are provided in a previous study (Goodale et al., 2020).

## **Zebrafish calcium imaging**

Data were acquired at Janelia Research Campus, Howard Hughes Medical Institute. Light-sheet calcium imaging recordings were made from fictively swimming larval zebrafish embedded in agarose. The fish swam against a fixed-velocity one-dimensional moving stripe pattern, which represented virtual water flow. The imaging spanned almost all brain neurons expressing a genetically encoded calcium indicator (GCaMP6f). Additional experimental  
525 details for these data are provided in a previous study (Mu et al., 2019).

## **Details of data preprocessing**

### **Intracranial EEG**

Dynamical stability analyses were performed on recordings sampled at 1000Hz, in accordance with previous work (Alonso et al., 2019; Solovey et al., 2015). All other analyses were  
530 performed on intracranial EEG data downsampled to 250Hz. All our results were robust to analysis and modeling of data at 1000Hz, but this higher sampling rate incurred unnecessary computational cost.

All recordings were highpass filtered with a cutoff of 0.5Hz using the `bandpassfilter` function from Fieldtrip toolbox (Oostenveld et al., 2011). In addition, macaque electrocortigraphy data were notch-filtered at 50Hz and 100Hz to remove line noise. Likewise, human  
535 stereotactic EEG and intracranial EEG data were notch-filtered at 60Hz and 120Hz to remove line noise.

## Calcium imaging

All images were motion corrected, and cells were segmented in contiguous and overlapping  
540 three-dimensional blocks, using non-negative matrix factorization with sparseness constraints.  
The resulting demixed and denoised cell segmentations showed high signal-to-noise ratio relative to raw pixel timeseries. Additional details of segmentation were provided in a previous study (Mu et al., 2019). Our segmentation software is publicly available from

<https://github.com/mikarubi/voluseg>

## 545 Details of data analysis

### Dynamical stability analysis

We performed linearized dynamical stability analysis within temporally local time windows. We first divided the timeseries  $\mathbf{v} \in \mathcal{R}^{n \times t}$ , into non-overlapping windows of length  $\Delta t = 500\text{ms}$  (Solovey et al., 2015). We then fitted a time-invariant vector autoregressive model, representing a linear dynamical system, separately for each window  $\mathbf{v}_{\mathbf{k}} \in \mathcal{R}^{n \times \Delta t}$ , where  $\mathbf{k}$  is a vector of timepoints within a window. The vector autoregressive model is defined as,

$$\mathbf{v}_{\mathbf{k}+1} = \mathbf{A}_{\mathbf{k}} \mathbf{v}_{\mathbf{k}}$$

For each window, we first estimated the system matrix  $\mathbf{A}_{\mathbf{k}} \in \mathcal{R}^{n \times n}$  using least squares (Neumaier & Schneider, 2001), and then computed its eigenvalues,  $\mathbf{z}_{\mathbf{k}} \in \mathcal{C}^{n \times 1}$ . These eigenvalues tracked the dynamical stability of this system. Specifically, the presence of all eigenvalues  
550 strictly inside the complex unit circle ( $|\mathbf{z}_{\mathbf{k}}^j| < 1$ , for  $j = 1, 2, \dots, n$ ) implies that the system is asymptotically stable, such that external perturbations will decay exponentially. In contrast, the presence of some eigenvalues outside the complex unit circle ( $|\mathbf{z}_{\mathbf{k}}^j| > 1$ ) implies that the system is unstable and that external perturbations will grow exponentially. Finally, the presence of eigenvalues on the complex unit circle ( $|\mathbf{z}_{\mathbf{k}}^j| \approx 1$ ), implies that the system is  
555 weakly stable and external perturbations will produce diverse responses (Solovey et al., 2015).

## Power spectral analysis

We used Welch’s method to characterize the power spectral density over a relatively large frequency range between 1 and 80Hz. In brief, power spectra were computed for each channel separately, using windowed timeseries convolved with Hanning windows of length 30 seconds and then averaged over all windows.

There has been significant recent progress in the development of methods for estimating slopes of neural power spectra. Unlike earlier methods, such as coarse grained spectral analysis (He et al., 2010), which were strictly applicable only to completely aperiodic signals (Wen & Liu, 2016), more recent methods, such as IRASA (Wen & Liu, 2016) and Fitting Oscillations and One Over f (FOOOF) (Donoghue et al., 2020), are able to estimate both periodic and aperiodic signal components.

Here, we adopted FOOOF to estimate the spectral exponent of empirical and model timeseries. Formally the algorithm estimates,

$$P(f) = \frac{10^{f_{\text{offset}}}}{(f + f_{\text{knee}})^e}$$

where  $P$  is the power spectrum,  $f$  is the frequency of interest,  $e$  is the scaling exponent,  $f_{\text{offset}}$  is the offset frequency, and  $f_{\text{knee}}$  is the knee frequency (Donoghue et al., 2020). More details about the application of this method to the study of neural spectra is provided in a recent study (Waschke et al., 2021). In this study, we set the maximum number of peaks to 6, and the minimum peak height to 0.15.

## Long range temporal correlation analysis

Following initial preprocessing, we bandpass filtered the data in the alpha (8-12Hz) and beta (20-30Hz) frequency bands, and applied the Hilbert transform to extract time-resolved amplitude at each electrode. We then used detrended fluctuation analysis to estimate amplitude scaling coefficients from these time-resolved amplitude timeseries (Peng et al., 1995). Detrended fluctuation analysis is especially suitable for analysis of neurophysiological timeseries because it is unaffected by nonstationary structure. In practice, given a timeseries  $y^j \in \mathcal{R}^{1 \times t}$ , we first

defined the cumulative sum  $\mathbf{Y}^j$  as follows,

$$\mathbf{Y}_i^j = \sum_{i=1}^t (y_i^j - t\bar{y}^j).$$

where  $\bar{y}^j$  denotes the mean activity of node  $j$ . We then segmented the timeseries into non-overlapping segments of varying lengths  $\Delta t$ . We considered a broad range of temporal windows, from 1 second to 3 minutes, in order to robustly capture scaling behavior across multiple timescales.

For each timescale  $\Delta t$ , we computed  $F(\Delta t)$ , the root-mean-square of the detrended cumulative signal  $\mathbf{Y}^j$  within each segment, averaged over segments. Finally, we fitted a power law of the form  $F(\Delta t) = h\Delta t^\alpha$ . The value of the exponent  $\alpha$  denotes the presence or absence of long-range temporal correlations. A value between 0.5 and 1.0 is indicative of long range temporal correlations, while values close to 0.5 denote an uncorrelated process.

### **Avalanche analysis**

*Avalanche detection in electrophysiological datasets.* Inline with previous studies, we binarized electrophysiological imaging datasets by setting to 1 deflections in local field potentials that exceeded three standard deviations below the mean (J. M. Palva et al., 2013; Solovey et al., 2012; Varley et al., 2020). We then detected, at each timepoint, bursts of temporally contiguous coordinated activity in these binarized timeseries. Specifically, a new avalanche is instantiated if at least one of the constituent elements becomes active. The avalanche propagates until none of the constituent elements are active. The size of an avalanche is defined by the number of active constituent elements, and the duration of an avalanche is defined by the period of its activity.

*Avalanche detection in calcium imaging datasets.* Inline with previous studies, we binarized calcium imaging datasets by setting to 1 deflections in calcium concentration that exceeded three standard deviations above the mean (Ponce-Alvarez et al., 2018). The standard method for avalanche detection fails for brain-wide cellular resolution data because the large number of cells produce a single never-ending avalanche. Inline with recent work, we used a method to detect spatially contiguous avalanches from binarized zebrafish calcium imaging

timeseries (Ponce-Alvarez et al., 2018). More specifically, we detected clusters of simultaneously active and spatially contiguous neurons. We used the MATLAB function `bwconncomp` to find these clusters. We then formed neuronal avalanches by detecting clusters that shared cells at adjacent timepoints. In this way, we followed the spatiotemporal structure of each avalanche as it started, propagated and ended.

*Power law fitting to avalanche distributions.* We assessed the presence of power-law scaling in avalanche distributions, by adopting methods described in (Clauset et al., 2009) and previously implemented in (Rubinov et al., 2011). Specifically, we denoted the probability density function of avalanche size as  $p(s)$ ,

$$p(s) = \frac{s^{-\tau}}{\zeta(\tau, s_{\min}) - \zeta(\tau, s_{\max} + 1)}$$

with a cumulative distribution function

$$P(s) = \frac{\zeta(\tau, s) - \zeta(\tau, s_{\max} + 1)}{\zeta(\tau, s_{\min}) - \zeta(\tau, s_{\max} + 1)}$$

where  $s$  is avalanche size,  $\tau$  is the scaling exponent,  $s_{\min}$  and  $s_{\max}$  are the lower and upper cut-off sizes and  $\zeta(\tau, s) = \sum_{i=0}^{\infty} (i + s)^{-\tau}$  is the generalized Hurwitz zeta function. The functions incorporate an upper cut-off  $s_{\max}$  because all empirical distributions are necessarily bounded by system size (Beggs & Plenz, 2003). We defined the probability distributions for avalanche durations  $l$  in exactly the same way. We then estimated the exponents of avalanche sizes and durations using the method of maximum likelihood, as previously described (Clauset et al., 2009; Rubinov et al., 2011).

*Exponent scaling and shape collapses.* We quantified power-law exponents between mean avalanche size for a given avalanche duration. We estimated the slope of this power law using linear regression in log-log coordinates (Friedman et al., 2012). Finally, we quantified avalanche shape collapses by averaging all avalanches of a given duration in a single recording. We rescaled collapsed avalanche shapes to have unit area and avalanche durations to have length 1.

## References

- Ahrens, M. B., Orger, M. B., Robson, D. N., Li, J. M., & Keller, P. J. (2013). Whole-brain functional imaging at cellular resolution using light-sheet microscopy. *Nature Methods*, *10*(5), 413–420.
- 620 Alonso, L. M., Proekt, A., Schwartz, T. H., Pryor, K. O., Cecchi, G. A., & Magnasco, M. O. (2014). Dynamical criticality during induction of anesthesia in human ecog recordings. *Frontiers in Neural Circuits*, *8*, 20.
- Alonso, L. M., Solovey, G., Yanagawa, T., Proekt, A., Cecchi, G. A., & Magnasco, M. O. (2019). Single-trial classification of awareness state during anesthesia by measuring  
625 critical dynamics of global brain activity. *Scientific Reports*, *9*(1), 1–11.
- Avery, M. C., & Krichmar, J. L. (2017). Neuromodulatory systems and their interactions: A review of models, theories, and experiments. *Frontiers in neural circuits*, *11*, 108.
- Bargmann, C. I. (2012). Beyond the connectome: How neuromodulators shape neural circuits. *Bioessays*, *34*(6), 458–465.
- 630 Bedard, C., Kroeger, H., & Destexhe, A. (2006). Does the 1/f frequency scaling of brain signals reflect self-organized critical states? *Physical Review Letters*, *97*(11), 118102.
- Beggs, J. M., & Plenz, D. (2003). Neuronal avalanches in neocortical circuits. *Journal of Neuroscience*, *23*(35), 11167–11177.
- Beggs, J. M., & Plenz, D. (2004). Neuronal avalanches are diverse and precise activity patterns that are stable for many hours in cortical slice cultures. *Journal of Neuroscience*,  
635 *24*(22), 5216–5229.
- Beggs, J. M., & Timme, N. (2012). Being critical of criticality in the brain. *Frontiers in Physiology*, *3*, 163.
- Bialek, W. (2017). Perspectives on theory at the interface of physics and biology. *Reports on  
640 Progress in Physics*, *81*(1), 012601.
- Breakspear, M. (2017). Dynamic models of large-scale brain activity. *Nature Neuroscience*, *20*(3), 340–352.
- Buzsáki, G. (2004). Large-scale recording of neuronal ensembles. *Nature Neuroscience*, *7*(5), 446–451.

- 645 Buzsáki, G., & Mizuseki, K. (2014). The log-dynamic brain: How skewed distributions affect network operations. *Nature Reviews Neuroscience*, *15*(4), 264–278.
- Chaudhuri, R., He, B. J., & Wang, X.-J. (2018). Random recurrent networks near criticality capture the broadband power distribution of human ecog dynamics. *Cerebral Cortex*, *28*(10), 3610–3622.
- 650 Chaudhuri, R., Knoblauch, K., Gariel, M.-A., Kennedy, H., & Wang, X.-J. (2015). A large-scale circuit mechanism for hierarchical dynamical processing in the primate cortex. *Neuron*, *88*(2), 419–431.
- Chialvo, D. R. (2010). Emergent complex neural dynamics. *Nature Physics*, *6*(10), 744–750.
- Churchland, M. M., Cunningham, J. P., Kaufman, M. T., Foster, J. D., Nuyujukian, P., Ryu, S. I., & Shenoy, K. V. (2012). Neural population dynamics during reaching. *Nature*, *487*(7405), 51–56.
- 655 Clauset, A., Shalizi, C. R., & Newman, M. E. (2009). Power-law distributions in empirical data. *SIAM Review*, *51*(4), 661–703.
- Cocchi, L., Gollo, L. L., Zalesky, A., & Breakspear, M. (2017). Criticality in the brain: A synthesis of neurobiology, models and cognition. *Progress in Neurobiology*, *158*, 132–152.
- 660 Colombo, M. A., Napolitani, M., Boly, M., Gosseries, O., Casarotto, S., Rosanova, M., Brichant, J.-F., Boveroux, P., Rex, S., Laureys, S., et al. (2019). The spectral exponent of the resting eeg indexes the presence of consciousness during unresponsiveness induced by propofol, xenon, and ketamine. *Neuroimage*, *189*, 631–644.
- 665 Cunningham, J. P., & Byron, M. Y. (2014). Dimensionality reduction for large-scale neural recordings. *Nature Neuroscience*, *17*(11), 1500–1509.
- Deco, G., Jirsa, V. K., & McIntosh, A. R. (2011). Emerging concepts for the dynamical organization of resting-state activity in the brain. *Nature Reviews Neuroscience*, *12*(1), 43–56.
- 670 Demas, J., Manley, J., Tejera, F., Kim, H., Traub, F. M., Chen, B., & Vaziri, A. (2021). High-speed, cortex-wide volumetric recording of neuroactivity at cellular resolution using light beads microscopy. *bioRxiv*.

- Destexhe, A., & Touboul, J. (2021). Is there sufficient evidence for criticality in cortical systems? *eNeuro*, 8(2).
- 675
- Donoghue, T., Haller, M., Peterson, E. J., Varma, P., Sebastian, P., Gao, R., Noto, T., Lara, A. H., Wallis, J. D., Knight, R. T., et al. (2020). Parameterizing neural power spectra into periodic and aperiodic components. *Nature Neuroscience*, 23(12), 1655–1665.
- Elsayed, G. F., & Cunningham, J. P. (2017). Structure in neural population recordings: An expected byproduct of simpler phenomena? *Nature Neuroscience*, 20(9), 1310–1318.
- 680
- Ezaki, T., Dos Reis, E. F., Watanabe, T., Sakaki, M., & Masuda, N. (2020). Closer to critical resting-state neural dynamics in individuals with higher fluid intelligence. *Communications Biology*, 3(1), 1–9.
- Friedman, N., Ito, S., Brinkman, B. A., Shimono, M., DeVille, R. L., Dahmen, K. A., Beggs, J. M., & Butler, T. C. (2012). Universal critical dynamics in high resolution neuronal avalanche data. *Physical Review Letters*, 108(20), 208102.
- 685
- Gao, R., Peterson, E. J., & Voytek, B. (2017). Inferring synaptic excitation/inhibition balance from field potentials. *Neuroimage*, 158, 70–78.
- Gao, R., van den Brink, R. L., Pfeffer, T., & Voytek, B. (2020). Neuronal timescales are functionally dynamic and shaped by cortical microarchitecture. *eLife*, 9, e61277.
- 690
- Gireesh, E. D., & Plenz, D. (2008). Neuronal avalanches organize as nested theta-and beta/gamma-oscillations during development of cortical layer 2/3. *Proceedings of the National Academy of Sciences*, 105(21), 7576–7581.
- Goodale, S. E., González, H. F., Johnson, G. W., Gupta, K., Rodriguez, W. J., Shults, R., Rogers, B. P., Rolston, J. D., Dawant, B. M., Morgan, V. L., et al. (2020). Resting-state seeg may help localize epileptogenic brain regions. *Neurosurgery*, 86(6), 792–801.
- 695
- Hahn, G., Petermann, T., Havenith, M. N., Yu, S., Singer, W., Plenz, D., & Nikoli, D. (2010). Neuronal avalanches in spontaneous activity in vivo. *Journal of Neurophysiology*, 104(6), 3312–3322.
- 700
- Haimovici, A., Tagliazucchi, E., Balenzuela, P., & Chialvo, D. R. (2013). Brain organization into resting state networks emerges at criticality on a model of the human connectome. *Physical Review Letters*, 110(17), 178101.

- He, B. J. (2014). Scale-free brain activity: Past, present, and future. *Trends in Cognitive Sciences*, 18(9), 480–487.
- 705 He, B. J., Zempel, J. M., Snyder, A. Z., & Raichle, M. E. (2010). The temporal structures and functional significance of scale-free brain activity. *Neuron*, 66(3), 353–369.
- Honey, C. J., Thesen, T., Donner, T. H., Silbert, L. J., Carlson, C. E., Devinsky, O., Doyle, W. K., Rubin, N., Heeger, D. J., & Hasson, U. (2012). Slow cortical dynamics and the accumulation of information over long timescales. *Neuron*, 76(2), 423–434.
- 710 Johnson, E. (2018). Intracranial eeg recordings of medial temporal, lateral frontal, and orbitofrontal regions in 10 human adults performing a visuospatial working memory task. <https://doi.org/10.6080/K0VX0DQD>
- Johnson, E., Adams, J. N., Solbakk, A.-K., Endestad, T., Larsson, P. G., Ivanovic, J., Meling, T. R., Lin, J. J., & Knight, R. T. (2018). Dynamic frontotemporal systems process space and time in working memory. *PLOS Biology*, 16(3), e2004274.
- 715 Jonas, E., & Kording, K. P. (2017). Could a neuroscientist understand a microprocessor? *PLoS Computational Biology*, 13(1), e1005268.
- Jones, B. E. (2005). From waking to sleeping: Neuronal and chemical substrates. *Trends in pharmacological sciences*, 26(11), 578–586.
- 720 Kato, S., Kaplan, H. S., Schrödel, T., Skora, S., Lindsay, T. H., Yemini, E., Lockery, S., & Zimmer, M. (2015). Global brain dynamics embed the motor command sequence of *Caenorhabditis elegans*. *Cell*, 163(3), 656–669.
- Kinouchi, O., & Copelli, M. (2006). Optimal dynamical range of excitable networks at criticality. *Nature Physics*, 2(5), 348–351.
- 725 Krakauer, J. W., Ghazanfar, A. A., Gomez-Marin, A., MacIver, M. A., & Poeppel, D. (2017). Neuroscience needs behavior: Correcting a reductionist bias. *Neuron*, 93(3), 480–490.
- Laub, A. J. (2005). *Matrix analysis for scientists and engineers* (Vol. 91). Siam.
- Lee, S.-H., & Dan, Y. (2012). Neuromodulation of brain states. *Neuron*, 76(1), 209–222.
- Lendner, J. D., Helfrich, R. F., Mander, B. A., Romundstad, L., Lin, J. J., Walker, M. P., Larsson, P. G., & Knight, R. T. (2020). An electrophysiological marker of arousal level in humans. *eLife*, 9, e55092.
- 730

- Liegeois, R., Laumann, T. O., Snyder, A. Z., Zhou, J., & Yeo, B. T. (2017). Interpreting temporal fluctuations in resting-state functional connectivity mri. *Neuroimage*, *163*, 437–455.
- 735 Linkenkaer-Hansen, K., Nikouline, V. V., Palva, J. M., & Ilmoniemi, R. J. (2001). Long-range temporal correlations and scaling behavior in human brain oscillations. *Journal of Neuroscience*, *21*(4), 1370–1377.
- Magnasco, M. O., Piro, O., & Cecchi, G. A. (2009). Self-tuned critical anti-hebbian networks. *Physical Review Letters*, *102*(25), 258102.
- 740 Marder, E. (2012). Neuromodulation of neuronal circuits: Back to the future. *Neuron*, *76*(1), 1–11.
- Maturana, M. I., Meisel, C., Dell, K., Karoly, P. J., DSouza, W., Grayden, D. B., Burkitt, A. N., Jiruska, P., Kudlacek, J., Hlinka, J., et al. (2020). Critical slowing down as a biomarker for seizure susceptibility. *Nature Communications*, *11*(1), 1–12.
- 745 Mu, Y., Bennett, D. V., Rubinov, M., Narayan, S., Yang, C.-T., Tanimoto, M., Mensh, B. D., Looger, L. L., & Ahrens, M. B. (2019). Glia accumulate evidence that actions are futile and suppress unsuccessful behavior. *Cell*, *178*(1), 27–43.
- Murray, J. D., Bernacchia, A., Freedman, D. J., Romo, R., Wallis, J. D., Cai, X., Padoa-Schioppa, C., Pasternak, T., Seo, H., Lee, D., et al. (2014). A hierarchy of intrinsic timescales across primate cortex. *Nature Neuroscience*, *17*(12), 1661–1663.
- 750 Nagasaka, Y., Shimoda, K., & Fujii, N. (2011). Multidimensional recording (mdr) and data sharing: An ecological open research and educational platform for neuroscience. *PLOS ONE*, *6*(7), e22561.
- Neumaier, A., & Schneider, T. (2001). Estimation of parameters and eigenmodes of multi-  
755 variate autoregressive models. *ACM Transactions on Mathematical Software (TOMS)*, *27*(1), 27–57.
- Oostenveld, R., Fries, P., Maris, E., & Schoffelen, J.-M. (2011). Fieldtrip: Open source software for advanced analysis of meg, eeg, and invasive electrophysiological data. *Computational Intelligence and Neuroscience*, *2011*.

- 760 Palva, J. M., Zhigalov, A., Hirvonen, J., Korhonen, O., Linkenkaer-Hansen, K., & Palva, S.  
(2013). Neuronal long-range temporal correlations and avalanche dynamics are corre-  
lated with behavioral scaling laws. *Proceedings of the National Academy of Sciences*,  
*110*(9), 3585–3590.
- Palva, S., & Palva, J. M. (2012). Discovering oscillatory interaction networks with m/eeg:  
765 Challenges and breakthroughs. *Trends in Cognitive Sciences*, *16*(4), 219–230.
- Palva, S., & Palva, J. M. (2018). Roles of brain criticality and multiscale oscillations in tempo-  
ral predictions for sensorimotor processing. *Trends in Neurosciences*, *41*(10), 729–743.
- Parvizi, J., & Kastner, S. (2018). Promises and limitations of human intracranial electroen-  
cephalography. *Nature Neuroscience*, *21*(4), 474–483.
- 770 Peng, C.-K., Havlin, S., Stanley, H. E., & Goldberger, A. L. (1995). Quantification of scaling  
exponents and crossover phenomena in nonstationary heartbeat time series. *Chaos*,  
*5*(1), 82–87.
- Petermann, T., Thiagarajan, T. C., Lebedev, M. A., Nicolelis, M. A., Chialvo, D. R., & Plenz,  
D. (2009). Spontaneous cortical activity in awake monkeys composed of neuronal  
775 avalanches. *Proceedings of the National Academy of Sciences*, *106*(37), 15921–15926.
- Peterson, E. J., Rosen, B. Q., Campbell, A. M., Belger, A., & Voytek, B. (2017). 1/f neural  
noise is a better predictor of schizophrenia than neural oscillations. *bioRxiv*, 113449.
- Ponce-Alvarez, A., Jouary, A., Privat, M., Deco, G., & Sumbre, G. (2018). Whole-brain neu-  
ronal activity displays crackling noise dynamics. *Neuron*, *100*(6), 1446–1459.
- 780 Prichard, D., & Theiler, J. (1994). Generating surrogate data for time series with several si-  
multaneously measured variables. *Physical Review Letters*, *73*(7), 951.
- Raut, R. V., Snyder, A. Z., Mitra, A., Yellin, D., Fujii, N., Malach, R., & Raichle, M. E. (2021).  
Global waves synchronize the brains functional systems with fluctuating arousal. *Sci-  
ence Advances*, *7*(30), eabf2709.
- 785 Roberts, J. A., Boonstra, T. W., & Breakspear, M. (2015). The heavy tail of the human brain.  
*Current Opinion in Neurobiology*, *31*, 164–172.
- Rubinov, M. (2016). Constraints and spandrels of interareal connectomes. *Nature Communica-  
tions*, *7*(1), 1–11.

- Rubinov, M., Sporns, O., Thivierge, J.-P., & Breakspear, M. (2011). Neurobiologically realistic determinants of self-organized criticality in networks of spiking neurons. *PLoS Computational Biology*, 7(6), e1002038.
- Saggar, M., Sporns, O., Gonzalez-Castillo, J., Bandettini, P. A., Carlsson, G., Glover, G., & Reiss, A. L. (2018). Towards a new approach to reveal dynamical organization of the brain using topological data analysis. *Nature Communications*, 9(1), 1–14.
- Saxena, S., & Cunningham, J. P. (2019). Towards the neural population doctrine. *Current Opinion in Neurobiology*, 55, 103–111.
- Schnider, T. W., Minto, C. F., Shafer, S. L., Gambus, P. L., Andresen, C., Goodale, D. B., & Youngs, E. J. (1999). The influence of age on propofol pharmacodynamics. *Anesthesiology*, 90(6), 1502–1516.
- Sethna, J. P., Dahmen, K. A., & Myers, C. R. (2001). Crackling noise. *Nature*, 410(6825), 242–250.
- Shew, W. L., Yang, H., Petermann, T., Roy, R., & Plenz, D. (2009). Neuronal avalanches imply maximum dynamic range in cortical networks at criticality. *Journal of Neuroscience*, 29(49), 15595–15600.
- Shine, J. M., Breakspear, M., Bell, P. T., Martens, K. A. E., Shine, R., Koyejo, O., Sporns, O., & Poldrack, R. A. (2019). Human cognition involves the dynamic integration of neural activity and neuromodulatory systems. *Nature Neuroscience*, 22(2), 289–296.
- Shriki, O., Alstott, J., Carver, F., Holroyd, T., Henson, R. N., Smith, M. L., Coppola, R., Bullmore, E., & Plenz, D. (2013). Neuronal avalanches in the resting meg of the human brain. *Journal of Neuroscience*, 33(16), 7079–7090.
- Smith, R. L. (1984). Efficient monte carlo procedures for generating points uniformly distributed over bounded regions. *Operations Research*, 32(6), 1296–1308.
- Solovey, G., Alonso, L. M., Yanagawa, T., Fujii, N., Magnasco, M. O., Cecchi, G. A., & Proekt, A. (2015). Loss of consciousness is associated with stabilization of cortical activity. *Journal of Neuroscience*, 35(30), 10866–10877.
- Solovey, G., Miller, K. J., Ojemann, J., Magnasco, M. O., & Cecchi, G. A. (2012). Self-regulated dynamical criticality in human ecog. *Frontiers in Integrative Neuroscience*, 6, 44.

- Stringer, C., Pachitariu, M., Steinmetz, N., Reddy, C. B., Carandini, M., & Harris, K. D. (2019). Spontaneous behaviors drive multidimensional, brainwide activity. *Science*, 364(6437).
- 820 Stumpf, M. P., & Porter, M. A. (2012). Critical truths about power laws. *Science*, 335(6069), 665–666.
- Touboul, J., & Destexhe, A. (2010). Can power-law scaling and neuronal avalanches arise from stochastic dynamics? *PLOS ONE*, 5(2), e8982.
- Touboul, J., & Destexhe, A. (2017). Power-law statistics and universal scaling in the absence  
825 of criticality. *Physical Review E*, 95(1), 012413.
- Trautmann, E. M., Stavisky, S. D., Lahiri, S., Ames, K. C., Kaufman, M. T., OShea, D. J., Vyas, S., Sun, X., Ryu, S. I., Ganguli, S., et al. (2019). Accurate estimation of neural population dynamics without spike sorting. *Neuron*, 103(2), 292–308.
- Varley, T. F., Sporns, O., Puce, A., & Beggs, J. (2020). Differential effects of propofol and  
830 ketamine on critical brain dynamics. *PLOS Computational Biology*, 16(12), e1008418.
- Voytek, B., & Knight, R. T. (2015). Dynamic network communication as a unifying neural basis for cognition, development, aging, and disease. *Biological Psychiatry*, 77(12), 1089–1097.
- Voytek, B., Kramer, M. A., Case, J., Lepage, K. Q., Tempesta, Z. R., Knight, R. T., & Gazzaley, A. (2015). Age-related changes in 1/f neural electrophysiological noise. *Journal of  
835 Neuroscience*, 35(38), 13257–13265.
- Waschke, L., Donoghue, T., Fiedler, L., Smith, S., Garrett, D. D., Voytek, B., & Obleser, J. (2021). Modality-specific tracking of attention and sensory statistics in the human electrophysiological spectral exponent (M. Chait, B. G. Shinn-Cunningham, B. R. Postle, & J. Z. Simon, Eds.). *eLife*, 10, e70068. <https://doi.org/10.7554/eLife.70068>
- 840 Wen, H., & Liu, Z. (2016). Separating fractal and oscillatory components in the power spectrum of neurophysiological signal. *Brain Topography*, 29(1), 13–26.
- Wohrer, A., Humphries, M. D., & Machens, C. K. (2013). Population-wide distributions of neural activity during perceptual decision-making. *Progress in Neurobiology*, 103, 156–193.  
845

Yanagawa, T., Chao, Z. C., Hasegawa, N., & Fujii, N. (2013). Large-scale information flow in conscious and unconscious states: An ecog study in monkeys. *PLOS ONE*, 8(11), e80845.

Zimmern, V. (2020). Why brain criticality is clinically relevant: A scoping review. *Frontiers in Neural Circuits*, 14, 54.

850

## Supplementary Files

This is a list of supplementary files associated with this preprint. Click to download.

- [tresosmoopapersicompressed.pdf](#)